Supporting Information

Melt processed perovskite glass-ceramic films for large-area X-ray detection and imaging

Peng Wang,†[a] Da Liu,†[a] Zhanpeng Wei,[a] Yuhao Zhao,[a] Haonan Wang,[a] Sihan Zeng,[a] Yuchen Zhu,[a] Yichu Zheng,[b] Yu Peng,[a] Yu Hou*[a] and Shuang Yang*[a]

Experimental Section

Materials: Lead bromide ($PbBr_2$, 99.0%), cesium bromide (CsBr, 99.5%), 4-(ethylaminomethyl)pyridine (4-EAMP, 99%), hydrobromic acid (HBr, 48% in water), and dimethyl sulfoxide (DMSO, 99.8%) were purchased from Shanghai Aladdin Biochemical Technology Co. All reagents were used directly without further purification.

Synthesis of $CsPbBr_3$ single crystals: $PbBr_2$ (7.0464 g, 19.2 mmol) and CsBr (2.043 g, 9.6 mmol) were dissolved in 10 mL DMSO. The mixture was then heated and stirred at 80 °C on a hot plate until the formation of a clear precursor solution. Then volatilize and crystallize at 80 °C.

Synthesis of $(4\text{-EAMP})_2Pb_3Br_{10}$ single crystals: $PbBr_2$ (1.1 g**,** 3 mmol) and 4-EAMP (0.28 g, 2 mmol) were dissolved in 5 mL HBr in a beaker at room temperature. The mixture was then heated and stirred at 120 °C on a hot plate until the formation of a clear precursor solution. The $(4\text{-EAMP})_2Pb_3Br_{10}$ single crystals were obtained by cooling the precursor solution to room temperature.

Fabrication of glass-ceramic film: $CsPbBr_3$ (7 g) and $(4\text{-EAMP})_2Pb_3Br_{10}$ (3 g) were placed in the agate ball milling jar for half an hour of ball milling to obtain a well-mixed composite powder. Preheat the silicon wafers and ITO glass sheets on a hot table at 230 ℃, and then evenly spread the composite powder on the ITO glass substrate. After the powder melts, cover the preheated silicon wafer on the surface of the melt and apply pressing. After two minutes, reduce the temperature to room temperature. Glass-ceramic composited films can be obtained by removing the silicon wafers.

Material Characterizations: X-ray diffraction (XRD) was carried out on Bruker Advance D8 X-ray diffractometer with Cu Kα radiation (40 kV, 40 mA). Thermogravimetry analysis (TGA) was performed on Netzsch TG 209F1 Libra instrument. Samples were heated from room temperature to 600 ℃ with a heating rate of 10 ℃ min^{-1} under nitrogen flow. Differential scanning calorimetry (DSC) analysis was carried out on Netzsch DSC 214 instrument at a heating rate of 10 ℃ min^{-1} under a nitrogen flow. Absorption spectra of the wafers were measured by an Ultraviolet-

visible (UV-vis) spectrophotometer (Jindao UV-2600). Transmission electron microscopy (TEM) characterization was conducted using Thermo Fisher Talos F200X microscope under 200 kV. High angle annular dark field (HAADF)-STEM images were performed on a convergence semi-angle of 11 mrad, and inner- and outer-collection angles of 59 and 200 mrad, respectively. Energy dispersive X-ray spectroscopy (EDS) was measured using four in-column Super-X detectors. Scanning electron microscopy (SEM) images were collected using field emission scanning electron microscopy (FESEM, HITACHI S4800). The Fourier transform infrared spectroscopy (FT-IR) was recorded using a PerkinElmer Frontier spectrophotometer. Micro computed tomography (Micro-CT) tests were conducted on the ZEISS Xradia 620 Versa. Laser confocal microscopy tests were conducted on the Nikon A1R. The time-of-flight secondary ion mass spectrometry test was conducted on TOF-SIMS 5 in the positive ion mode. The melt viscosity test was conducted on NETZSCH Kinexus Lab$^+$ in plate mode. The tensile test was conducted on the CMT6103.

Photoelectronic characterization: For $\mu\tau$ product measurement, a 405 nm LED as excitation light, was modulated at 50 Hz by a function generator. The photoconductivity current of the glass sample was recorded by using a Keithley 2400 digital source meter. The $\mu\tau$ value can be calculated by fitting the photoconductivity using the modified Hecht equation:

$$I = \frac{I_0 \mu\tau V 1 - exp(-\frac{L^2}{\mu\tau V})}{L^2 \quad 1 + \frac{Ls}{V\mu}}$$

where I_0 represents the saturation current, L is the material thickness, and V is the applied bias voltage.[1]

The trap density (N_{trap}) determined by the space-charges-limited-current (SCLC) method.[2] The trap-filled limit voltage (V_{TFL}), identified at the transition between the ohmic and trap-filled region, determines the trap density (N_{trap}), and it can be calculated by the following equation:

$$N_{trap} = \frac{2\varepsilon\varepsilon_0 V_{TFL}}{eL^2}$$

Where ε is the relative dielectric constant, ε_0 is the vacuum dielectric constant (8.85×10^{-12} F m^{-1}), e is the elementary charge, and L is the thickness of the wafer.

The electrical conductivity values of the samples were measured at various temperatures, and the activation energy for ion migration (E_a) was obtained through Nernst-Einstein equation:

$$\sigma(T) = \frac{\sigma_0}{T} exp\left(-\frac{E_a}{k_B T}\right)$$

where σ_0 is a constant, T is the temperature and k_B is the Boltzmann constant.[2]

X-ray detection measurement and imaging: During the X-ray detection experiment, the sample was exposed to an X-ray tube (Cu anode, Canon, A40) with a tube voltage of 40 kV. The dose rates were controlled by adjusting the tube current (2–40 mA) or using aluminum foil as attenuation layer, which was calibrated by a RaySafe X2 R/F sensor. The X-ray response current was measured using a Keithley 2400 digital source meter. The sensitivity (S) of the X-ray detector, defined as the response capability to the dose rate per unit area, can be calculated using the following formula:

$$S = \frac{I_p - I_d}{D * A}$$

where I_p is the photocurrent, I_d is the dark current, D is the dose rate, and A is the detection area.[3]

The dark current drift (I_{drift}) can be calculated according to the following equation:

$$I_{drift} = \frac{I_t - I_0}{E * S * t}$$

where I_t and I_0 are the current at the ending and beginning state, E is the applied electric field, S is the electrode area of the detector, and t is the duration time.[4]

The commonly used method based on the linear extrapolation of the dose-rate dependent SNR was also employed for comparison. The SNR is calculated using the following formula:

$$SNR = \frac{I_{signal}}{I_{noise}}$$

Where I_{signal} is the difference between the average photocurrent and the average dark

current and I_{noise} presents the standard deviation of the photocurrent.[5]

For X-ray imaging, a 3.3 × 3.3 cm glass-ceramic film was integrated onto the TFT substrate backplane (the TFT backplane and readout circuit system were provided by LinkZill) by hot-pressing method. Mixed powder of CPB and EPB was spread on the TFT backsheet and then heated to 230 ℃ to melt the powder. The film was obtained by hot pressing with silicon wafers. Finally, the top surface of the device was covered with 100 nm of silver as the top electrode. The flat-panel detector was operated under a 6.23 $\mu Gy_{air}\ s^{-1}$ dose rate with 15 V bias for imaging. The sample size of the pixel value distribution in the detector was 4096.

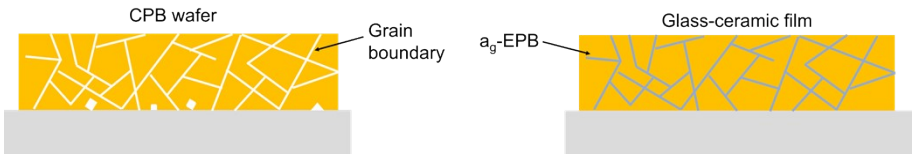

Fig. S1. Schematic diagram comparing the internal structures of CPB polycrystalline wafer and glass-ceramic films.

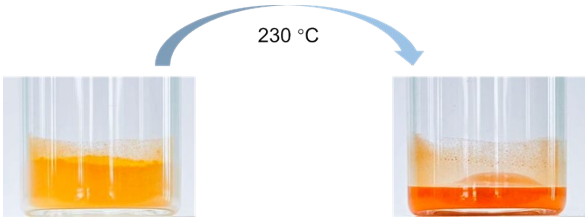

Fig. S2. Pictures of glass-ceramic composite before and after heating.

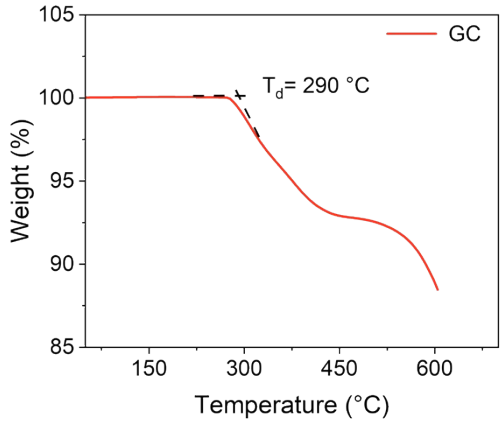

Fig. S3. TGA curve of glass-ceramic with a standard 10 °C min^{-1} ramping rate. The decomposition temperature of glass-ceramic was determined to be 290 °C.

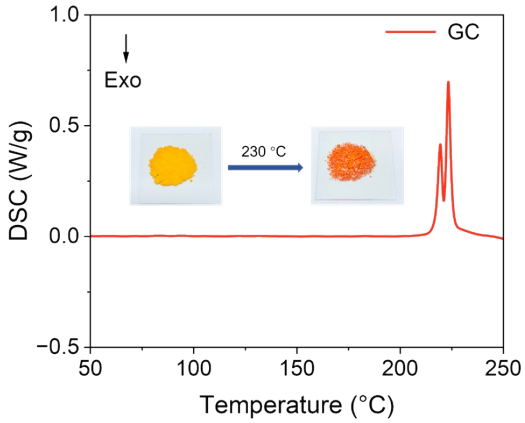

Fig. S4. DSC curve of glass-ceramic with a standard 10 °C min^{-1} ramping rate. The melting point was taken as the endothermic peak temperature.

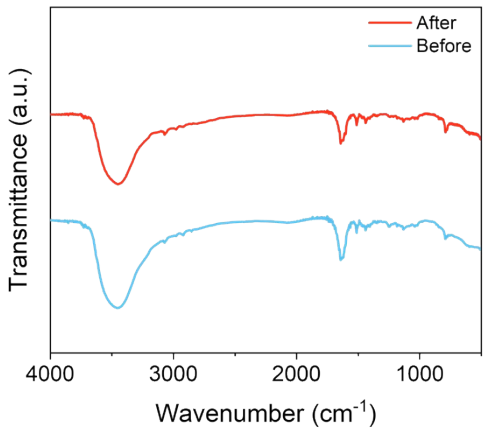

Fig. S5. The FT-IR spectra of glass-ceramic before and after heat treatment show consistent organic composition, demonstrating that no decomposition of EPB occurred during melt-processing.

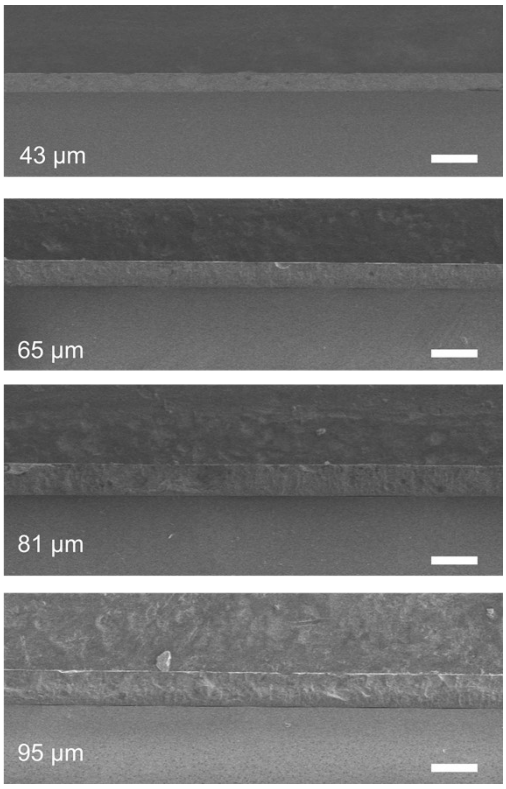

Fig. S6. Cross-sectional SEM images of glass-ceramic films with different thickness (Scale bars: 100 μm).

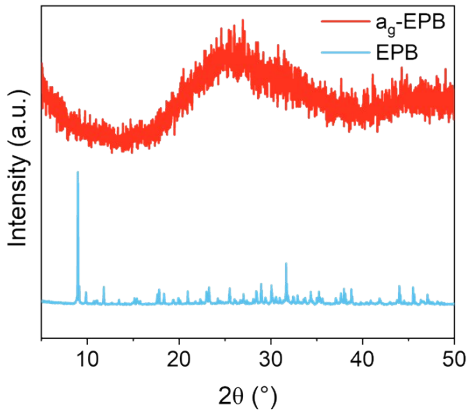

Fig. S7. XRD patterns of crystalline and amorphous $(4\text{-EAMP})_2Pb_3Br_{10}$.

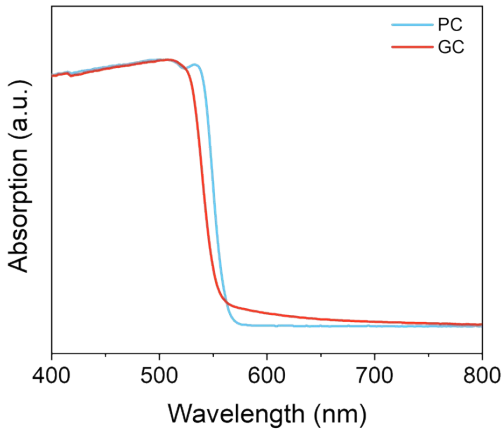

Fig. S8. UV-vis absorption patterns of CPB polycrystalline and glass-ceramic.

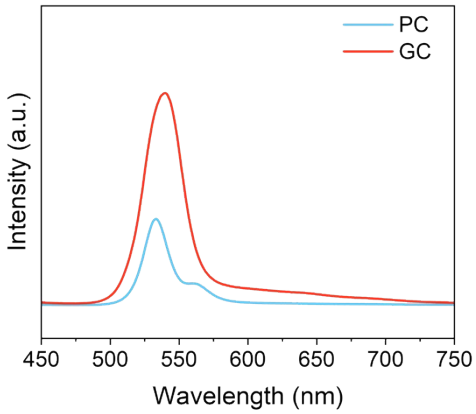

Fig. S9. Photoluminescence (PL) spectra of CPB polycrystalline and glass-ceramic.

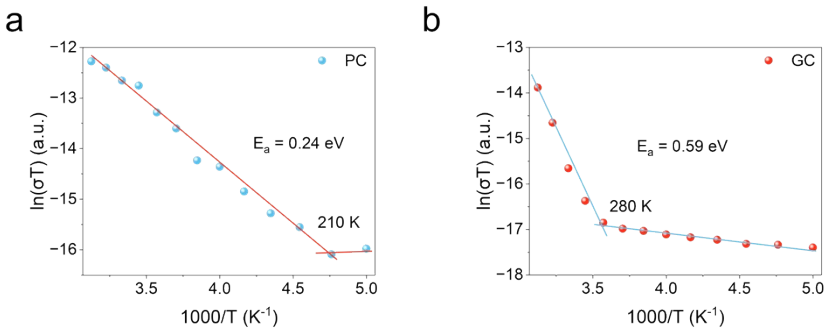

Fig. S10. Ion activation energies for the (a) CPB polycrystalline wafer and (b) glass-ceramic film.

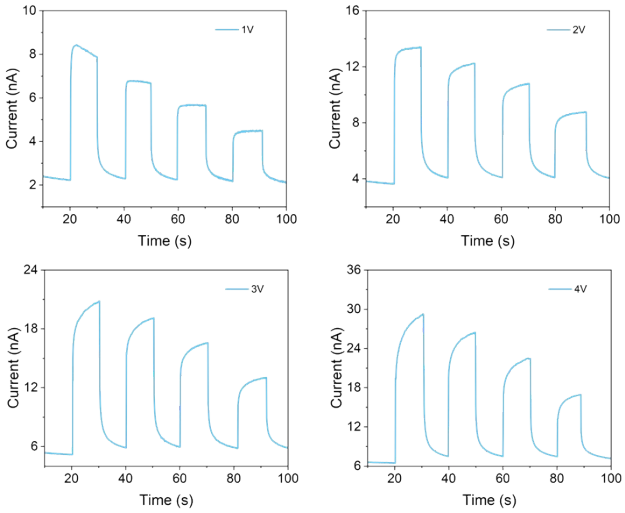

Fig. S11. Time-dependent response of CPB polycrystalline wafer device under varying X-ray dose rates and bias voltages.

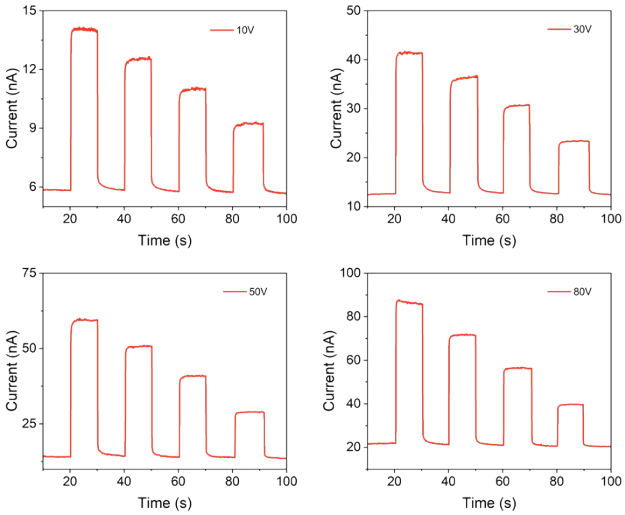

Fig. S12. Time-dependent response of the glass-ceramic detector under varying X-ray dose rates and bias voltages.

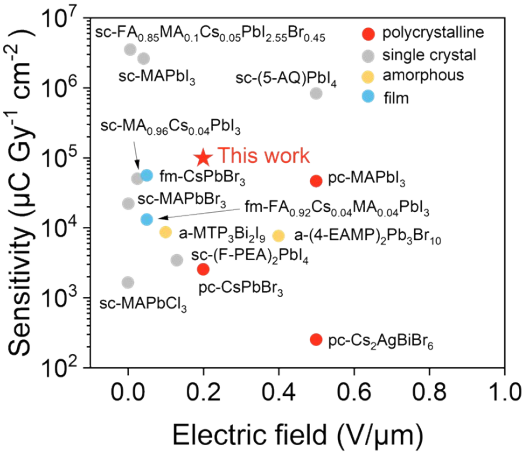

Fig. S13. Comparison of detection sensitivity as a function of electric field strength.

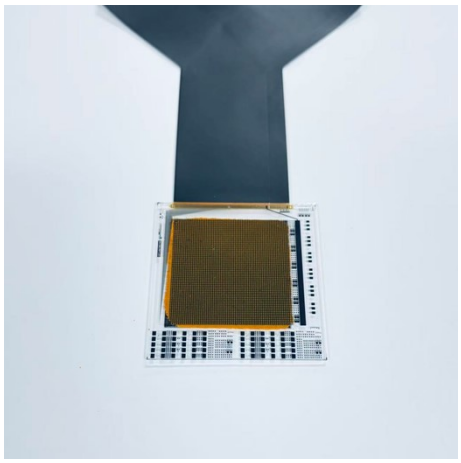

Fig. S14. A backside photo of the glass-ceramic film and TFT board integrated device.

Reference

1. H. Wei, Y. Fang, P. Mulligan, W. Chuirazzi, H.-H. Fang, C. Wang, B. R. Ecker, Y. Gao, M. A. Loi, L. Cao and J. Huang, *Nat. Photonics*, 2016, **10**, 333-339.
2. X. Zhao, Z. Li, S. Wang, Y. Song, E. Hong, T. Yan, G. Meng and X. Fang, *Adv Funct Mater*, 2025, **35**, 2500039.
3. D. Liu, W. Jiang, S. Dong, H. Di, H. Li, Z. Xing, H. Wang, J. Ren, X. Zheng, L. Lei and Y. Zhao, *Chem. Eng. J*, 2024, **495**, 153554.
4. M. Li, H. Li, W. Li, B. Li, T. Lu, X. Feng, C. Guo, H. Zhang, H. Wei and B. Yang, *Adv Mater*, 2022, **34**, 2108020.
5. D. Liu, F. Liao, H. Di, H. Li, S. Tie, J. Song, L. Lei and C. Chen, *Laser Photonics Rev*, 2025, **19**, 2400917.